

Moment tensor catalogue of ~~micro~~earthquakes in West Bohemia from 2008 to 2018

Václav Vavryčuk¹, Petra Adamová¹, Jana Doubravová¹, Josef Horálek¹

¹Institute of Geophysics, Boční II/1401, 14100 Praha 4, Czech Republic

Correspondence: Václav Vavryčuk (vv@ig.cas.cz)

Abstract

We present a unique catalogue of full moment tensors (MTs) of ~~micro~~earthquakes with M_L between 0.5 and 4.4 that occurred in West Bohemia, Czech Republic, in the period from 2008 to 2018. The MTs were calculated from vertical components of P-wave amplitudes. The MT inversion was based on the principal component analysis applied to optimally filtered velocity records of local seismic stations deployed in the West Bohemia area. The minimum number of inverted stations is 15 and the RMS between theoretical and observed amplitudes is lower than 0.5. The catalogue is exceptional in several aspects: (1) it represents an extraordinary extensive dataset of more than 5.000 MTs, (2) it covers a long period of seismicity in the studied area, during which several prominent earthquake swarms took place, (3) the locations and retrieved MTs of ~~micro~~earthquakes are of a high accuracy. Additionally, we provide three-component records at the West Bohemia (WEBNET) seismic stations, the velocity model in the region, and the technical specification of the stations. The dataset is ideal for being utilized by a large community of researchers for various seismological purposes, e.g., for studies of (1) the migration of foci and the spatiotemporal evolution of seismicity, (2) redistribution of stress during periods of intense seismicity, (3) the interaction of faults, (4) the Coulomb stress along the faults and local stress anomalies connected to fault irregularities, (5) diffusivity of fluids along the activated faults, or (6) the time-dependent seismic risk due to the migration of seismicity in the region. In addition, the dataset is optimum for developing and testing new inversions for MTs and for tectonic stress. Since most of the earthquakes are non-shear, the dataset can contribute to studies of non-double-couple components of MTs and their relation to shear-tensile fracturing and/or seismic anisotropy in the focal zone.

1 Introduction

The seismic moment tensor (MT) describes equivalent body forces acting at an earthquake source (Knopoff and Randall, 1970). It is a basic quantity evaluated for earthquakes that informs us about their moment magnitude, focal mechanism and type of faulting. It ~~is formed by~~ can be separated into double-couple (DC), isotropic (ISO) and compensated linear vector dipole (CLVD) components (Jost and Hermann, 1998; Vavryčuk, 2015). The DC component is produced by shear faulting in isotropic media; the ISO and CLVD components reflect complexities in the earthquake source, e.g., irregularly shaped faults, seismic anisotropy,

38 shear-tensile faulting induced by fluid injection in volcanic or geothermal areas, or the presence of a material
39 interface in the focal zone (Frohlich, 1994; Julian et al. 1998; Miller et al. 1998; Růžek et al., 2003; Šílený and
40 Milev, 2008; Vavryčuk 2005, 2006, 2011a, 2013, 2015; Vavryčuk and Hrubcová 2017).

41

42 Since earthquakes do not occur separately but in sequences, it is necessary to compile high-quality MT
43 catalogues for understanding origins of seismicity, tectonic stress regime and seismic energy release of any
44 region under study. In this way, we can identify prominent periods of seismicity, trace faults and fault
45 segments, monitor migration of earthquake foci, analyse interactions of nearby or intersecting faults, and map
46 the fluid flow along the fault systems in the focal zone (Vavryčuk et al., 2021). Hence, MT catalogues are
47 fundamental sources of information for all detailed studies of seismicity on the local, regional or global scale.

48

49 In this paper, we present recordings, locations and high-quality moment tensors of 51 ~~3482~~ **micro**earthquakes
50 that occurred in the West Bohemia geothermal region, Czech Republic in the period from 2008 to 2018. The
51 ~~micro~~earthquakes were monitored by the West Bohemia local seismic network WEBNET (Horálek et al.,
52 2000; Fischer et al., 2010). Their locations were calculated by the double-difference location method and the
53 moment tensors were determined using the moment tensor inversion of P waves based on the principal
54 component analysis. Because of its extent and quality, the presented dataset is unique and represents an
55 extraordinary dataset, which might find exciting applications in numerous future studies.

56

57 **2 West-Bohemia seismoactive region**

58 The region of West Bohemia is located in the western part of the Bohemian Massif, where three major tectonic
59 units are merged: the Saxothuringian, the Teplá-Barrandian and the Moldanubian. The region is
60 geodynamically active exposed to the Tertiary and Quaternary volcanism associated with CO₂ emanations,
61 dry and wet mofettes, and numerous mineral springs (Kämpf et al., 2013; Hrubcová et al., 2017; Bräuer et al.,
62 2018). Two major fault systems are identified in the area: the Mariánské Lázně fault striking in the NW-SE
63 direction and the Ore-Mountain fault striking in the WSW-ENE direction (Figure 1b). The recently most active
64 fault is, however, a left-lateral strike-slip fault in the N-S direction, situated at the eastern boundary of the Cheb
65 Basin filled by up to 300 m thick Tertiary and Quaternary sediments. The seismically active faults were
66 identified at depth by clustering of hypocentres and by focal mechanisms (Vavryčuk et al., 2013), but they also
67 have some geological evidence on the surface (Bankwitz et al., 2003).

68

69 The seismic energy in the West Bohemia region is typically released in the form of earthquake swarms. The
70 occurrence of the earthquake swarms has been well documented in the region since the beginning of the 19th
71 century. A significant increase of the earthquake activity was observed at the turn of the 19th and 20th century,
72 when several larger swarms were observed. There were earthquake swarms in 1897, 1900, 1903 and 1908.
73 During the last 40 years, the seismicity occurs in the area of 40 x 50 square kilometres, but the most intense
74 seismicity is focused in the Nový Kostel zone with size of 3 x 12 square kilometres (Fischer et al., 2014;
75 Čermáková and Horálek, 2015). Foci of ~~micro~~earthquakes in this zone are clustered along a fault striking in
76 the roughly N-S direction (Figure 1a) with depths ranging from 6 to 11 km. The duration of the earthquake

77 swarms varies; it lasts from several days for micro-swarms up to 2-3 months for the most prominent swarms.
 78 The swarms may consist of several thousands of **micro**earthquakes. The local magnitudes M_L of the
 79 **micro**earthquakes rarely exceed a value of 4.0. The strongest instrumentally recorded swarm activity occurred
 80 in 1985/86 with two main shocks having magnitudes of M_L 4.6 and 4.2.

81
82
83
84
85
86
87
88
89
90
91
92
93
94
95
96
97
98
99
100
101
102
103
104
105
106
107
108
109
110
111
112
113
114
115
116
117
118
119
120
121
122
123
124

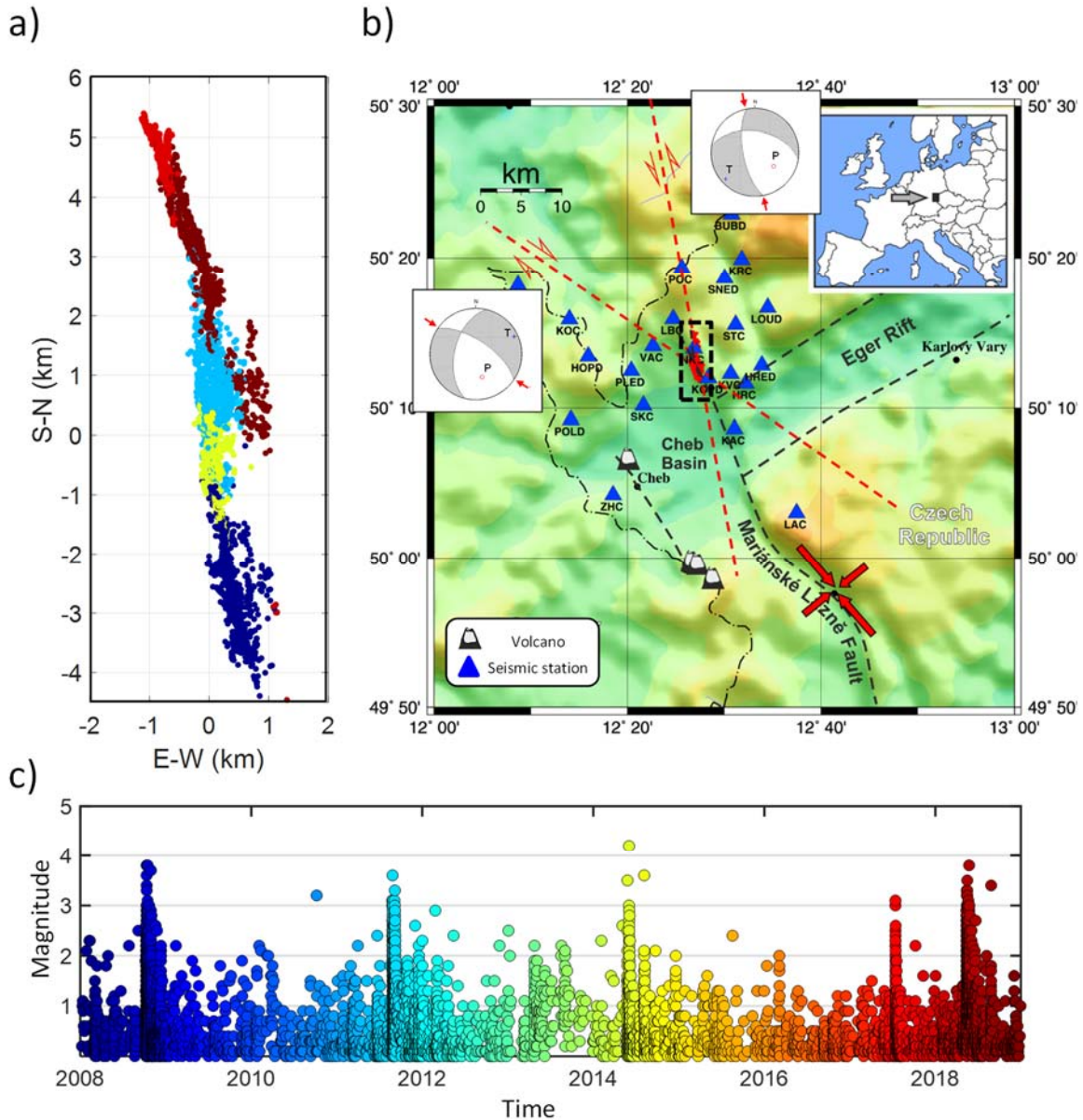


Figure 1. (a) The map view of earthquake foci in the period from 2008 to 2018, (b) topographic map with tectonic faults (black dashed lines) and positions of stations (blue triangles), and (c) the magnitude-time plot with the colour-coded time. The red dots in (b) show the earthquake foci. The dashed rectangle around the foci in (b) defines the area shown in panel (a). The red full arrows mark the orientation of the maximum and minimum principal stress axes. The dashed-dotted line marks the boundary between the Czech Republic and Germany. The position of West Bohemia in Europe is indicated in the inset. The focal mechanisms typical for the area are also indicated.

125 3 Monitoring system

126 The seismic activity in the region is monitored by the local seismic network WEBNET (Figure 1b, Table 1).
 127 The network ~~was is~~ operating since 1994 and the number of stations gradually increased (Horálek et al., 2000;
 128 Fischer et al., 2010). After its major upgrade in 2008, the WEBNET network consists of 23 seismic stations
 129 within the epicentral distance of 25 km. The stations cover the area ~~rather~~ uniformly with ~~a minor azimuthal~~
 130 ~~gap of 45° to the south~~~~no azimuthal gaps~~. The three component ground-velocity records are sampled at 250 Hz
 131 and the frequency response is flat at least between 1 and 80 Hz. Until September 2014, all data were processed
 132 based on triggered records. Since the beginning of September 2014, the recordings are processed by using
 133 automatic pre-processing of continuous recordings. Another major upgrade of the network was realized in
 134 2015. Originally, the stations were equipped by the Le-3DLite and SM3 seismometers; some of them were
 135 lately upgraded using the Guralp CMG-3ESP seismometers. The station with the nearest epicentral distance
 136 (station NKC) is additionally equipped with the broadband STS-2 seismometer. For a ~~detailed~~-technical
 137 specification of the WEBNET seismic stations, see Table 1. Full information on stations is provided in files
 138 Webnet.xml (formatted according to the FDSN StationXML standard,
 139 <http://docs.fdsn.org/projects/stationxml/en/latest/>) and Webnet.dataless (formatted according to the Dataless
 140 SEED format (<https://ds.iris.edu/ds/nodes/dmc/data/formats/dataless-seed/>) that are included in the dataset.

142 **Table 1.** Location and instrumentation of the WEBNET seismic stations
 143

Code	Site name	Latitude (°N)	Longitude (°E)	<i>h</i> (m)	Sensor before 2015	Digitizer before 2015	Sensor after 2015	Digitizer after 2015	Note
BUBD	Bublava	50.38174	12.51362	746	LE-3DLite	Gaia	LE-3DLite	Gaia	
HOPD	Horní Paseky	50.22378	12.26547	731	LE-3DLite	Gaia	LE-3DLite	Gaia	
HRC	Hrádek	50.19348	12.53660	596	LE-3DLite	Gaia	LE-3DLite	Gaia	Out of order from 2015
HRED	Hřebeny	50.21425	12.56491	589	LE-3DLite	Gaia	LE-3DLite	Gaia	<u>Timing problems in 2011 and 2014</u>
HUC	Komorní Hůrka	50.09997	12.33612	480	-	-	CMG-3ESPC	Taurus	Installed in 2016 ₂ , <u>anomalous site effects</u>
KAC	Kaceřov	50.14361	12.51708	548	SM-3	Janus-Trident	SM-3	Janus-Trident	
KOC	Kopaniny	50.26417	12.23288	621	SM-3	5800 PCM	CMG-3ESPC	Centaur	
KOPD	Kopanina	50.20319	12.47473	536	LE-3DLite	Gaia	LE-3DLite	Gaia	

KRC	Kraslice	50.33069	12.52950	806	SM-3	Janus-Trident	CMG-3ESPC	Centaur	
KVC	Květná	50.20496	12.51134	666	SM-3	5800 PCM	CMG-3ESPC	Centaur	
LAC	Lazy	50.04967	12.62396	884	SM-3	5800 PCM	CMG-3ESPC	Centaur	
LBC	Luby	50.26461	12.41123	684	SM-3	Janus-Trident	CMG-3ESPC	Centaur	
LOUD	Loučná	50.27753	12.57449	692	LE-3DLite	Gaia	LE-3DLite	Gaia	
NKC	Nový Kostel	50.23234	12.44706	610	SM-3 CMG-40T	5800 PCM Janus-Trident	CMG-3ESPC STS-2	Centaur	
PLED	Plesná	50.20890	12.33767	556	LE-3DLite	Gaia	LE-3DLite	Gaia	
POC	Počátky	50.31997	12.42662	841	SM-3	Janus-Trident	CMG-3ESPC	Centaur	
POLD	Polná	50.15603	12.23497	556	LE-3DLite	Gaia	LE-3DLite	Gaia	
SKC	Skalná	50.16911	12.36050	501	SM-3	Janus-Trident	CMG-3ESPC	Centaur	
SNED	Sněžná	50.31088	12.50131	756	LE-3DLite	Gaia	LE-3DLite	Gaia	
STC	Studenec	50.25794	12.51849	712	SM-3	Janus-Trident	CMG-3ESPC	Centaur	
TRC	Trojmezí	50.30344	12.14466	612	LE-3DLite	Gaia	CMG-3ESPC	Centaur	
VAC	Vackov	50.23450	12.37634	581	SM-3	Janus-Trident	CMG-3ESPC	Centaur	
ZHC	Zelená Hora	50.06984	12.30810	677	CMG-40T	Janus-Trident	CMG-3ESPC	Centaur	
MAC	Chlum sv. Maří	50.14429	12.53516	609	-	-	CMG-3ESPC	Centaur	Installed in 2017

144 Quantity h means the altitude of the stations. Recording systems: Taurus – Nanometrics digitizer; Janus-Trident
145 – Nanometrics communications controller-digitizer; Centaur – Nanometrics digitizer; Gaia – Vistec digitizer;
146 5800 PCM – Lennartz digitizing system. Seismometers: SM-3 – SP sensor; LE-3DLite – Lennartz SP sensor;
147 CMG-40T – Guralp BB sensor; CMG-3ESPC – Guralp BB sensor. Station HUC has anomalous site effects
148 and it was not used in the MT inversion. Time in station HRED is erroneously shifted by 0.45 s in 2011 and
149 by 2 s in 2014.

150
151

152 4 Seismicity in 2008-2018

153 The West Bohemia region is characterized by a continuous background seismicity scattered over the whole
154 region interrupted by earthquake swarm sequences located mostly in the Nový Kostel focal zone. The most

155 intense periods of seismicity are in 2008, 2011, 2014, 2017 and 2018 (Figures 1c and 2). All these sequences
 156 are typical earthquake swarms except for the seismic activity in 2014, which was exceptional. This sequence
 157 resembled a mainshock-aftershock sequence rather than the earthquake swarm (Hainzl et al., 2016; Jakoubková
 158 et al., 2018; Vavryčuk and Adamová, 2018) being formed by three pronounced activity periods. The strongest
 159 events in these periods reached magnitude significantly larger than the other events (Figure 2c). The seismic
 160 sequences differ in the earthquake productivity, in the duration, and in the number of periods of the intense
 161 seismicity (Figure 2). The strongest event in the period from 2008 to 2018 reached magnitude M_L of 4.2 and
 162 it occurred in 2014.

163

164

165

166

167

168

169

170

171

172

173

174

175

176

177

178

179

180

181

182

183

184

185

186

187

188

189

190

191

192

193

194

195

196

197

198

199

200

201

202

203

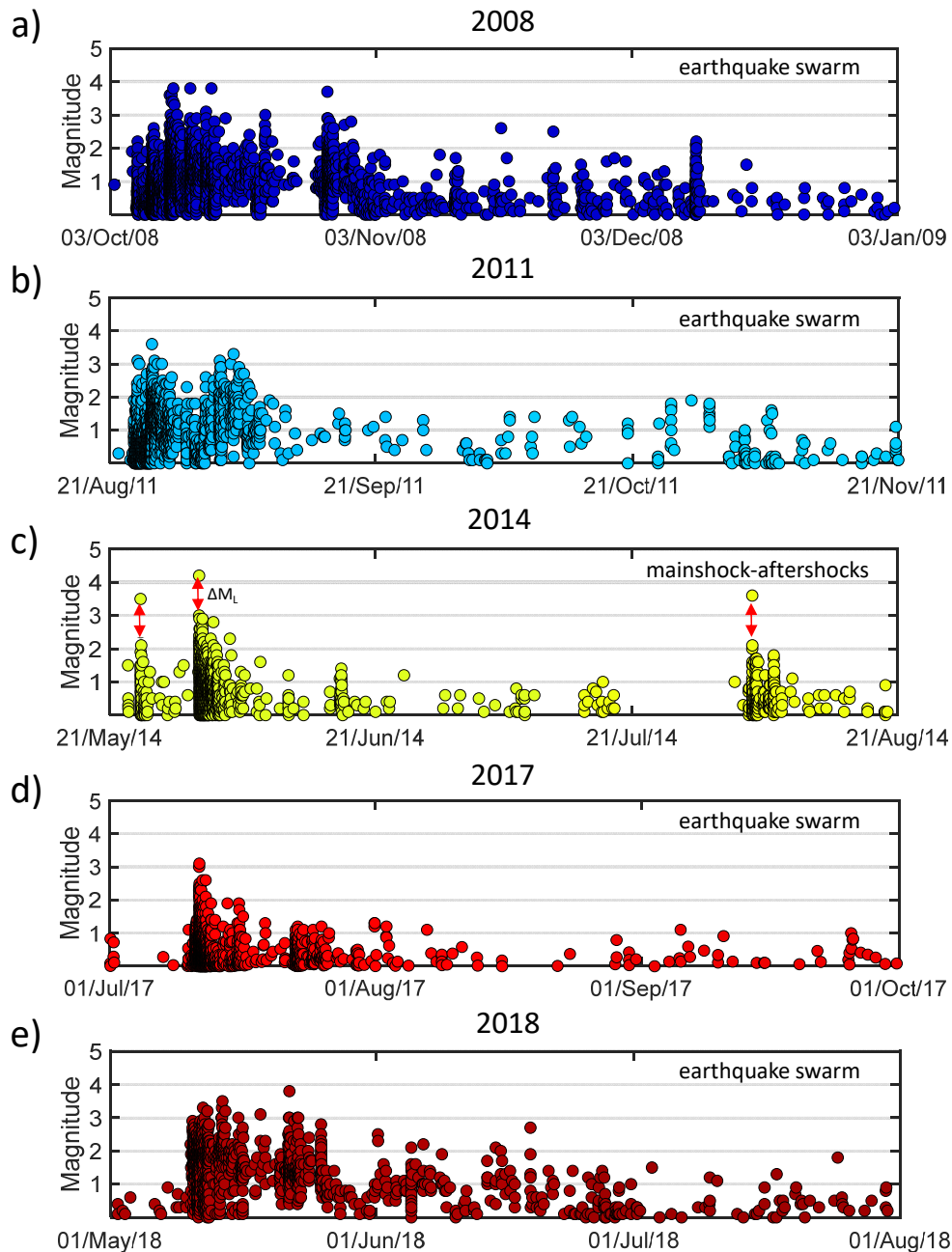


Figure 2. Magnitude-time plots of the major seismic sequences in the period from 2008 to 2018. According to the Bath law (Bath, 1965), the 2014 activity resembles rather a mainshock-aftershock sequence, because the difference in magnitudes ΔM_L between two strongest events in individual seismicity phases exceeds 1. In other seismic sequences, the magnitude gaps between two strongest events are not so prominent.

204

205 **5 Magnitudes and foci locations**

206 The local magnitude of earthquakes is computed from the velocity records according to the formula of Horálek
 207 et al. (2000). The locations are computed in two steps. First, initial locations were calculated by the NonLinLoc
 208 code (Lomax et al., 2009) in a layered velocity model (see Table 2) developed by Málek et al. (2005). For the
 209 locations, manual picks of the P and S arrivals were used. Second, we applied the double-difference location
 210 algorithm developed by Waldhauser and Ellsworth (2000) to differential times calculated from manual picks.
 211 The relative precision of hypocentres was less than ± 20 m within the cluster (Bouchaala et al., 2013). The
 212 absolute location of the cluster was determined with the accuracy of about ± 100 m in the horizontal plane and
 213 ± 350 m in depth (see Bouchaala et al., 2013).

214

215 The locations of foci point to complex geometry of the fault system in the focal area (Figure 3). The seismicity
 216 migrated from south to north in time and the individual seismic sequences occurred along different subfaults
 217 (Fischer et al., 2010; Bouchaala et al., 2013; Vavryčuk et al., 2013; Jakoubková et al., 2017). For example, the
 218 2008, 2011 and 2017 swarms activated three similarly oriented subfaults separated with gaps and offsets
 219 between them. The barrier between the fault segments activated in 2008 and 2011 was broken in 2014 (Hainzl
 220 et al., 2016; Vavryčuk and Adamová, 2018), and the gap between the fault segments activated in 2011 and
 221 2017 was broken during the 2018 swarm (Bachura et al., 2021; Vavryčuk et al., 2021). The overall direction
 222 of the whole fault system is defined by strike of 170° and dip of 75° . However, some fault segments may
 223 deviate from this overall direction significantly. For example, small echelon faults located at the deepest part
 224 of the fault system have strike of 305° and dip of 65° (see Figure 3c, blue dots at the depth range of 10.5-11
 225 km).

226

227

228

Table 2. The layered velocity model

Depth (km)	0.0	0.2	0.5	1.0	2.0	4.0	6.0	10.0	20.0	32.0
v_P (km/s)	4.30	5.06	5.33	5.60	5.87	6.09	6.35	6.74	7.05	7.25
Q_P	30	40	50	60	80	100	150	200	300	400

229

Ratio v_P/v_S is 1.70 and ratio Q_P/Q_S is 2.

231

232

233

234

235

236

237

238

239

240

241

242

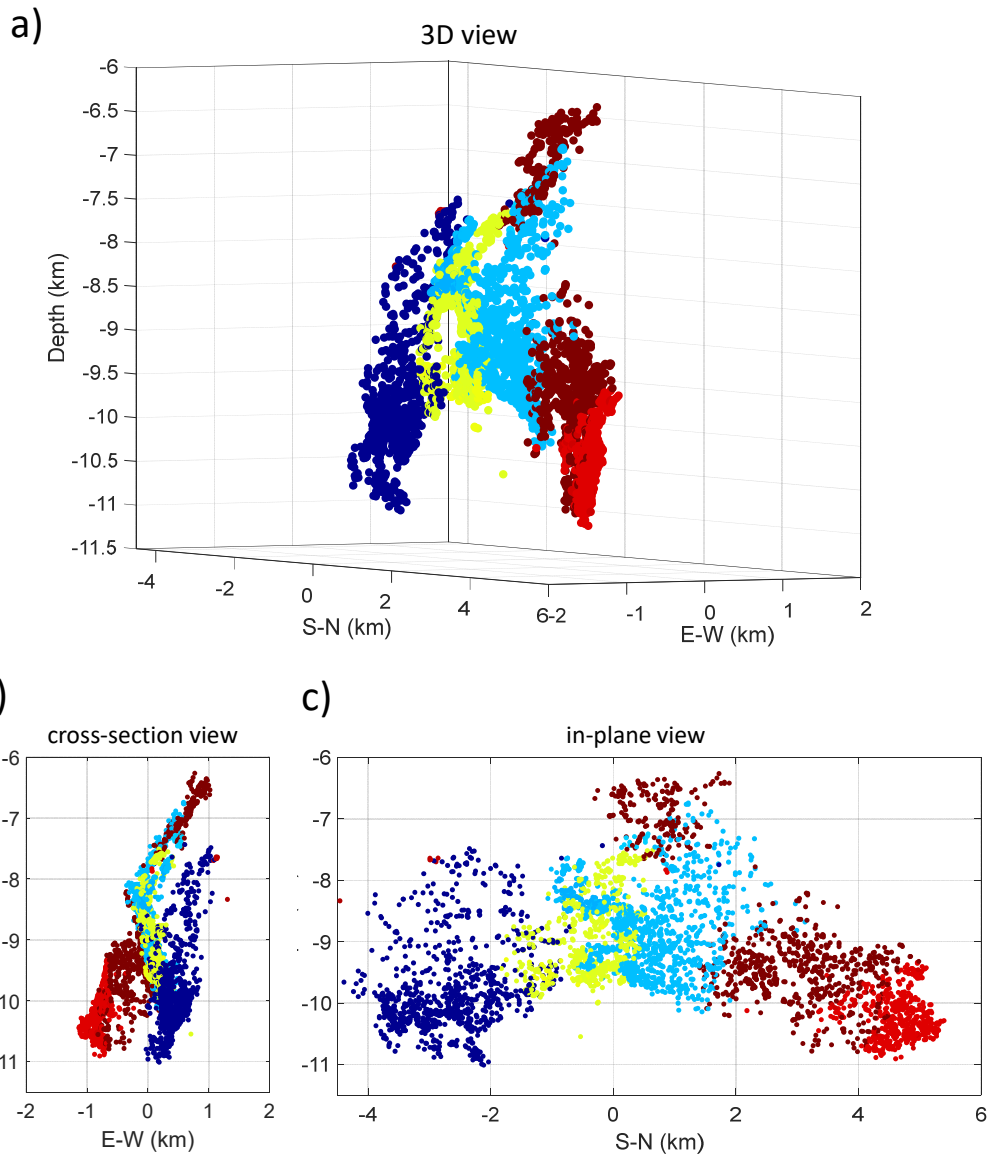


Figure 3. The earthquakes foci with local magnitude $M_L \geq 0.5$ in (a) 3D view, (b) cross-section vertical view, and (c) in-plane vertical view. The foci are colour coded according to time: dark blue – 2008, light blue – 2011, yellow – 2014, red – 2017, and brown – 2008.

6 Moment tensors

6.1 MT inversion of ~~micro~~earthquakes

The MT inversion requires accurate locations of earthquakes, an accurate crustal velocity model, dense coverage of stations on the focal sphere and low seismic noise (Šílený, 2009; Ford et al., 2010; Stierle, Bohnhoff, et al., 2014; Stierle, Vavryčuk, et al., 2014). We can invert amplitudes of seismic phases, amplitude ratios or full waveforms (Dreger and Woods, 2002; Cesca et al., 2006; Sokos and Zahradník, 2008; Cesca and Dahm, 2008; Vavryčuk et al., 2008; Zahradník et al., 2008; Fojtíková et al., 2010; Kwiatek et al., 2016; Jechumtálová and Šílený, 2005; Vavryčuk and Kühn, 2012; Yu et al., 2018, 2019). The applicability of the individual MT inversions is specific, depending on their applicability to earthquake of different magnitude

292 of analysed earthquakes, predominant wave frequencies and epicentral distances of stations. MTs of moderate
293 or large earthquakes are usually calculated from full waveforms recorded at regional or global seismic
294 networks. By contrast, MTs of small earthquakes and microearthquakes are commonly calculated from
295 amplitudes of P and/or S waves picked in short-period seismograms recorded at local networks. In this way,
296 the sensitivity of the MT inversion to small-scale complexities of the local geological structure are suppressed
297 and a computationally demanding modelling of high-frequency full waveforms is avoided.
298

299 The inversion for MTs of small earthquakes and microearthquakes is challenging for several reasons: (1) the
300 waveforms are complex due to high frequencies and noise, and (2) the datasets are extensive with thousands
301 of events, which require a semi- or fully-automated processing. Here, the MT inversion developed by Vavryčuk
302 et al. (2017) is applied. The inversion is based on the principal component analysis (PCA), which transforms
303 correlated waveforms into a set of the so called principal components (see Figure 4). The first component has
304 the highest variance and reproduces a so-called ‘common wavelet’, i.e., a wavelet with the highest similarity
305 with all analysed traces. This common wavelet physically represents a signal radiated by the earthquakes
306 source, which can be distorted during its propagation from the source to the receiver by inhomogeneities in
307 the geological structure, site effects or seismic noise.

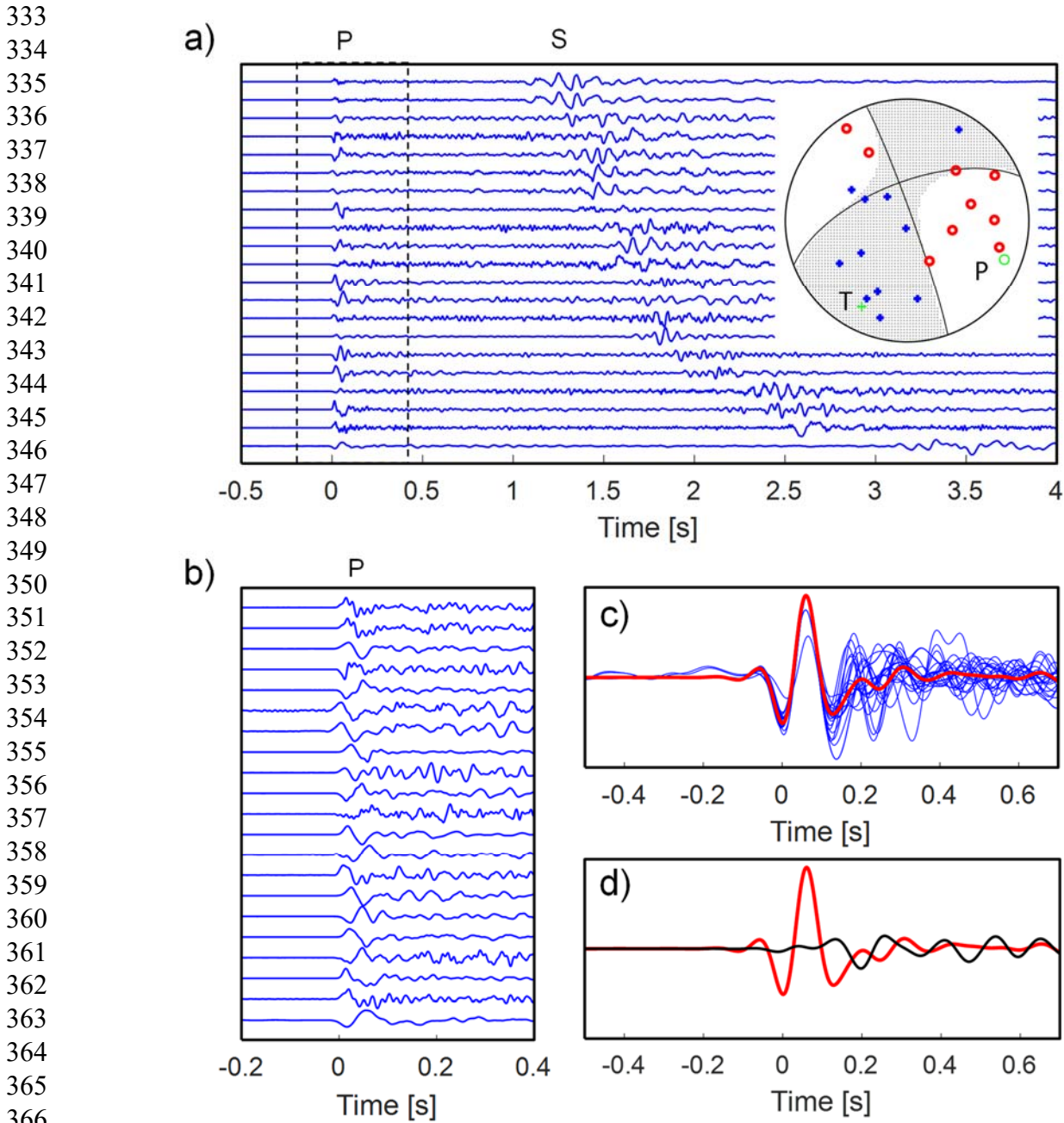
308
309 Subsequently, the common wavelet is correlated with individual recorded traces and the effective P-wave
310 amplitudes are calculated as the amplification factors applied to the common wavelet, in order to optimally
311 reproduce the recorded traces. The obtained amplitudes are inverted for the MTs using the generalized linear
312 inversion (Lay and Wallace, 1995). The Green’s function amplitudes are computed by the ray method
313 (Červený, 2001; Vavryčuk, 1999, 2008) and incorporated the effects of the Earth’s surface. An inhomogeneous
314 medium with a vertical gradient obtained by smoothing the layered model of Málek et al. (2005) was applied
315 for computing the rays by the ray-tracing algorithm. The inversion is robust, fast and insensitive to noise in
316 data.

317 318 319 **6.2 Individual steps of the MT inversion**

320 The MT inversion consists of data pre-processing, alignment of traces, computation of the effective amplitudes
321 using the PCA method and the MT inversion. The data are not corrected for the frequency response of sensors,
322 because the response is flat for all sensors at least from 2 to 60 Hz. The individual steps of the inversion are as
323 follows (see Figure 5):

- 324 1. Data pre-processing, which comprises: (a) an oversampling of records in order to perform an accurate
325 alignment of waveforms, (b) band-pass filtering to enhance the signal-to-noise ratio, and (c) a rough
326 alignment of waveforms using manual picks, if available, or using an automatic picking algorithm called
327 the Suspension Bridge Picking (SBPx), see FeedMeImATroll (2021).
- 328 2. Two-step accurate alignment of waveforms, which comprises: (a) an alignment of waveforms using the
329 cross-correlation with the waveform of the highest signal-to-noise ratio, (b) calculation of the first principal

330 component from the aligned waveforms, (c) another alignment of waveforms using the cross-correlation
 331 with the computed first principal component, and (d) calculation of the refined first principal component
 332 from the aligned waveforms.



368 **Figure 4.** Example of the MT inversion of the ~~micro~~earthquake on 24 May 2014 at 16:14:30 with ML 2.1. (a)
 369 Whole velocity records; (b) window with aligned P waves; (c) the common wavelet (red line) together with
 370 the P-wave traces at individual stations (blue lines); (d) the common wavelet represented by the first principal
 371 component (red line) and noise in waveforms represented by the second principal component (black line). The
 372 polarities of the P-wave in panel (c) are switched to be consistent with the polarity of the common wavelet.
 373 The inset in plot (a) shows the focal mechanism and positions of stations on the focal sphere (red circles mark
 374 negative polarities, and blue plus signs mark the positive polarities).

375

- 376 3. Calculation of the PCA amplitudes and weights in the MT inversion, which comprises: (a) calculation of
 377 the PCA coefficients of the first principal component, which serve as the effective amplitudes used in the
 378 MT inversion, (b) calculation of the correlation coefficients between individual traces and the first principal
 379 component, which serve as the weights in the linear MT inversion scheme (in this way, a station with a
 380 waveform significantly different from the common wavelet suppressed in the inversion),
- 381 4. Repeated MT inversion for several alternative band-pass filters and time windows, in order to adapt the
 382 inversion to earthquakes with a varying frequency content. The inversion is firstly run with the whole set
 383 of stations, and secondly with eliminating two stations producing the largest misfits in the inversion.

384 In this way, we obtain a set of candidate MTs. The optimum MT is that with the minimum root-mean-squares
 385 (RMS) of differences between the synthetic amplitudes A^{synth} and the observed amplitudes A^{obs}

$$386 \text{RMS} = \frac{\sqrt{\sum_{i=1}^N (A_i^{synth} - A_i^{obs})^2}}{\sqrt{\sum_{i=1}^N (A_i^{synth})^2}}, \quad (1)$$

387 where N is the number of stations. The optimum MT is normalized and expressed in a relative scale, because
 388 it is computed from wave amplitudes but not from full displacement records. The scalar moment is obtained
 389 by integrating the common (displacement) wavelet. The optimum MTs were further decomposed into the DC,
 390 ISO and CLVD components according to Equations (6-10) of Vavryčuk (2015).

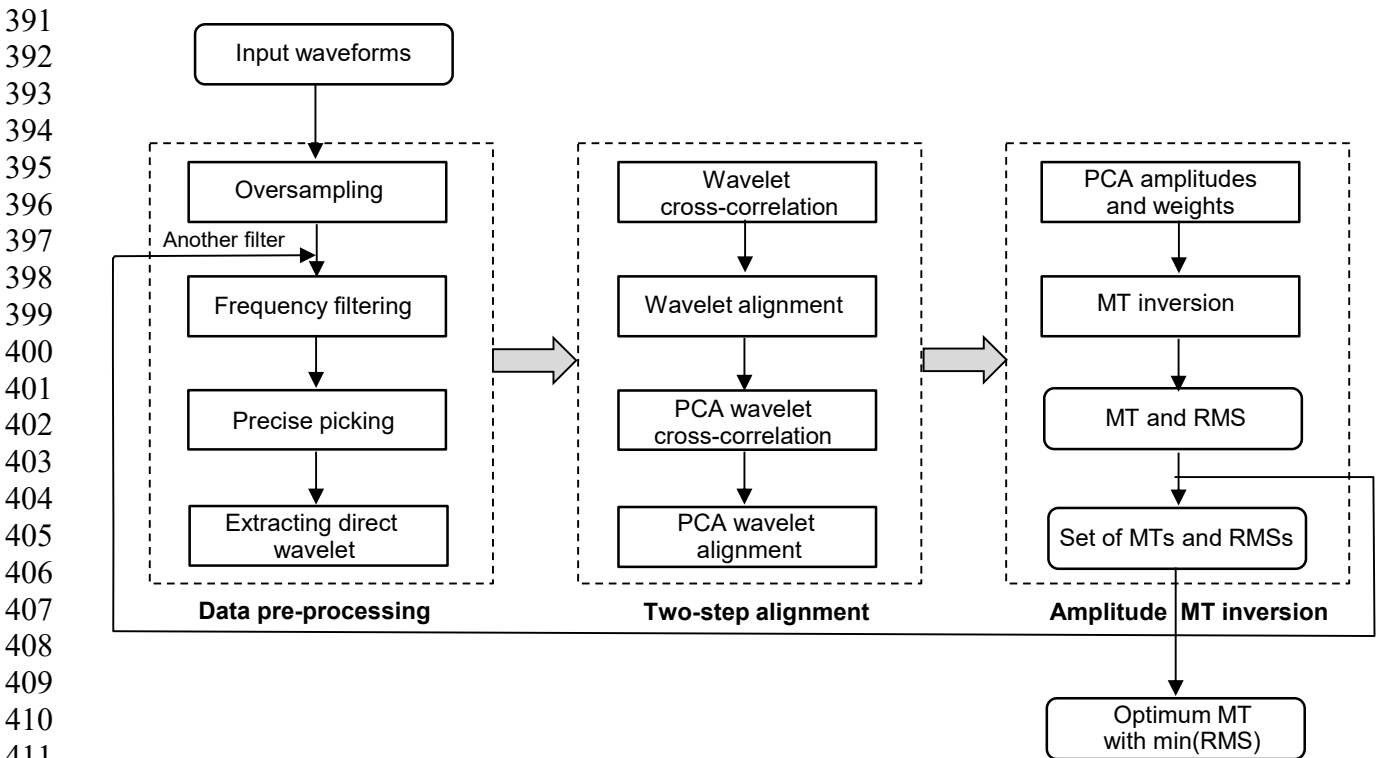


Figure 5. Flowchart of the PCA moment tensor inversion.

416
417
418
419
420
421
422
423
424
425
426
427
428
429
430
431
432
433
434
435
436
437
438
439
440
441
442
443
444
445
446
447
448
449
450
451
452
453
454
455
456
457
458
459
460
461
462
463
464
465
466
467
468
469

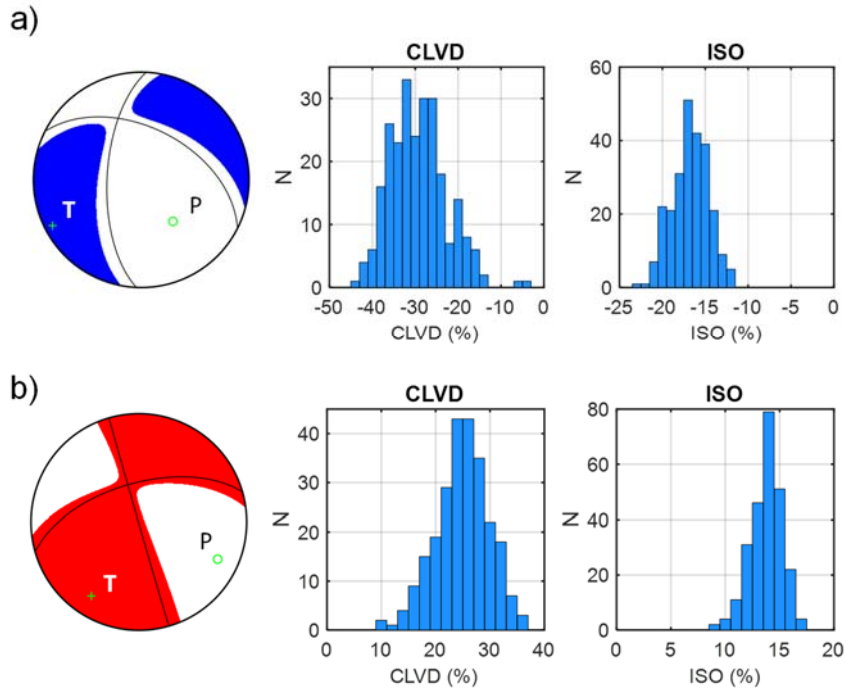


Figure 6. Examples of focal mechanisms and histograms of the CLVD and ISO errors. (a) EMicroearthquake on 1 September, 2011 at 12:54:05.7 with $ML = 0.6$, and (b) microearthquake on 11 May, 2018 at 06:26:09.0 with $ML = 2.3$.

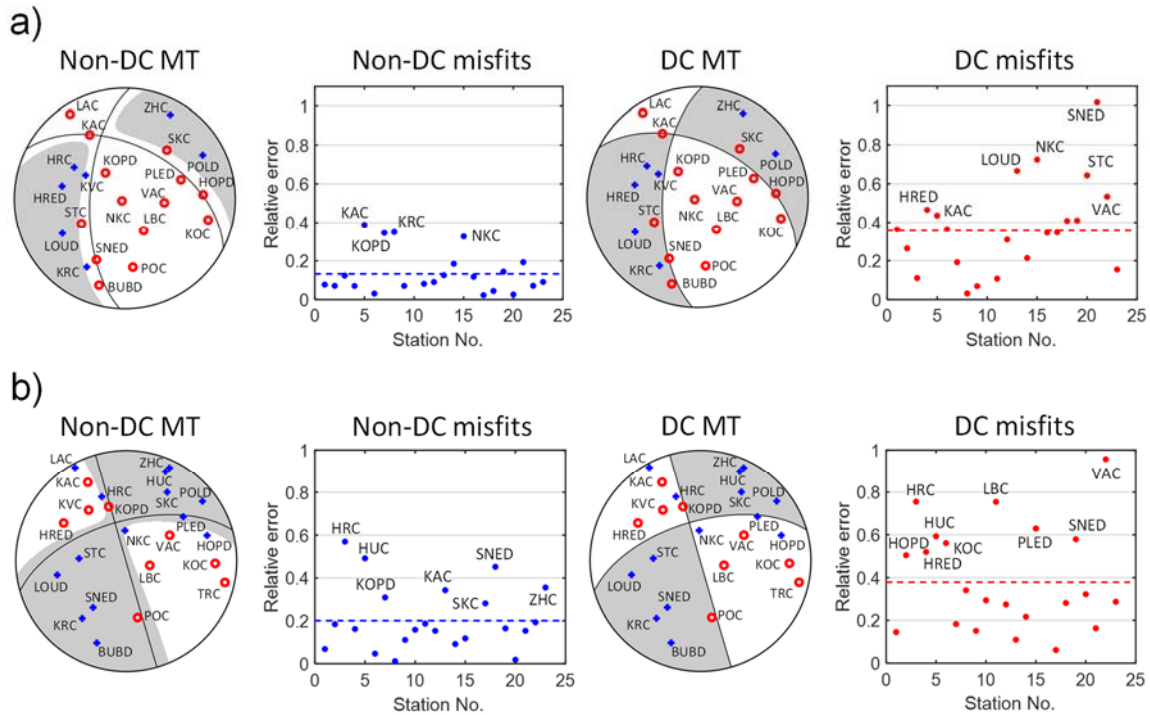


Figure 7. Inversion for the full MT solution (‘Non-DC MT’ and ‘Non-DC misfits’) and for the DC solution (‘DC MT’ and ‘DC misfits’) for microearthquakes in Figure 6. The mean amplitude misfits for the full MT and DC solutions are shown by blue and red dashed lines, respectively.

470
 471 In order to estimate errors of the MTs, the inversion is performed for each MT repeatedly 100 times using
 472 amplitudes distorted by noise characterized by a flat probability distribution. The level of noise ranges from
 473 $\pm 25\%$ to 25% of the inverted amplitude at each trace. The scatter of the solutions served for estimating: (1)
 474 the mean errors in the P/T axes directions calculated as the mean of deviations between the directions of the
 475 P/T axes of noise-free solution and the noisy solutions, (2) the mean errors in the percentages of the DC, ISO
 476 and CLVD components calculated as the standard deviations of the DC, ISO and CLVD values of noisy MT
 477 solutions.

478
 479 Figure 6 exemplifies the MT inversion for two ~~micro~~-earthquakes, which display significant non-DC
 480 components. The histograms of the CLVD and ISO errors indicate that the ISO component is always better
 481 constrained than the CLVD component. Nevertheless, despite the numerical errors produced by the inversion,
 482 the histograms prove that both the events contain also true non-DC components. This is also confirmed by a
 483 comparison of fits for the full MTs and for the DC solutions for the events shown in Figure 7. The figure
 484 indicates that the misfits for the full MT solutions are almost twice lower than those for the DC solutions. This
 485 proves that at least some part of the non-DC components retrieved by the MT inversion should be of physical
 486 origin.

487
 488

489 **7 Basic characteristics of the MT catalogue**

490 Firstly, we processed all events with the local magnitude larger than 0.5. After that, we checked manually the
 491 quality of input data and the retrieved MT and we excluded earthquakes: (1) recorded at a low number of
 492 stations ($N < 154$), (2) with extremely low signal-to-noise ratio, (3) produced unstable moment tensors with
 493 anomalously high RMS ($RMS > 0.54$). In this way, we obtained a dataset of 51~~3482~~ earthquakes listed in the
 494 catalogue. Table 3 summarizes the numbers of events in individual years. The magnitude-frequency
 495 distribution of the analysed events is shown in Figure 8.

496
 497
 498
 499

Table 3. Number of reported events for each year.

Year	2008	2009	2010	2011	2012	2013
Number of events	99 01	3840	249	12 1125	69	201
Year	2014	2015	2016	2017	2018	2008-2018
Number of events	83141	3640	3233	58 03	11 2230	51 3482

500
 501
 502
 503
 504

505
506
507
508
509
510
511
512
513
514
515
516
517
518
519
520
521
522
523
524
525
526
527
528
529
530
531
532
533
534
535
536
537
538
539
540
541
542
543
544
545
546
547
548
549
550

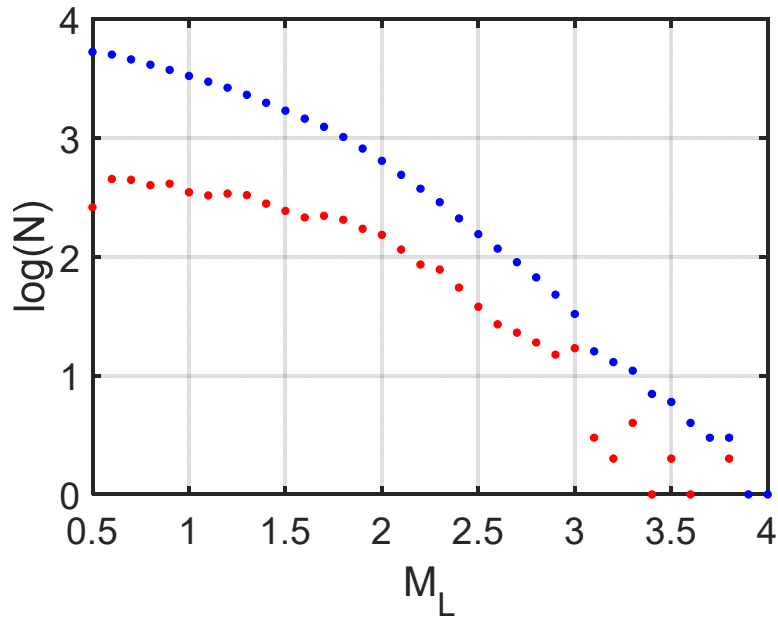


Figure 8. Cumulative (blue) and non-cumulative (red) magnitude-frequency distribution of the analysed earthquakes.

The earthquakes inverted for MTs were recorded mostly by 20 or more stations (Figure 9, middle column). The RMS varied during the whole period and ranged mostly from 0 to 0.5 (Figure 9, right column). The MTs with RMS higher than 0.5 were considered as unreliable. The variation of the RMS in time is probably produced by varying station coverage due to the foci migration. The P/T axes form compact and non-overlapping clusters for all seismic sequences in the studied time period (Figure 9). The position of clusters slightly differs in individual years and indicates some stress variation in the focal zone. Directions of the P/T axes are well resolved with the mean standard deviation less than 2° (Figure 10, two left columns). The errors of the ISO and CLVD components are mostly about 1.5-2% and 5-6%, respectively (Figure 10, two right columns). Comparing these errors for individual activity periods, we see that the errors tend to slightly decrease with time. This might be due to a continuously increasing quality of the WEBNET network. The histograms of the standard deviations of the P/T axes and the ISO and CLVD errors for the whole period from 2008-2018 are shown in Figure 11.

551
 552
 553
 554
 555
 556
 557
 558
 559
 560
 561
 562
 563
 564
 565
 566
 567
 568
 569
 570
 571
 572
 573
 574
 575
 576
 577
 578
 579
 580
 581
 582
 583
 584
 585
 586
 587
 588
 589
 590
 591
 592
 593
 594
 595
 596
 597
 598
 599
 600

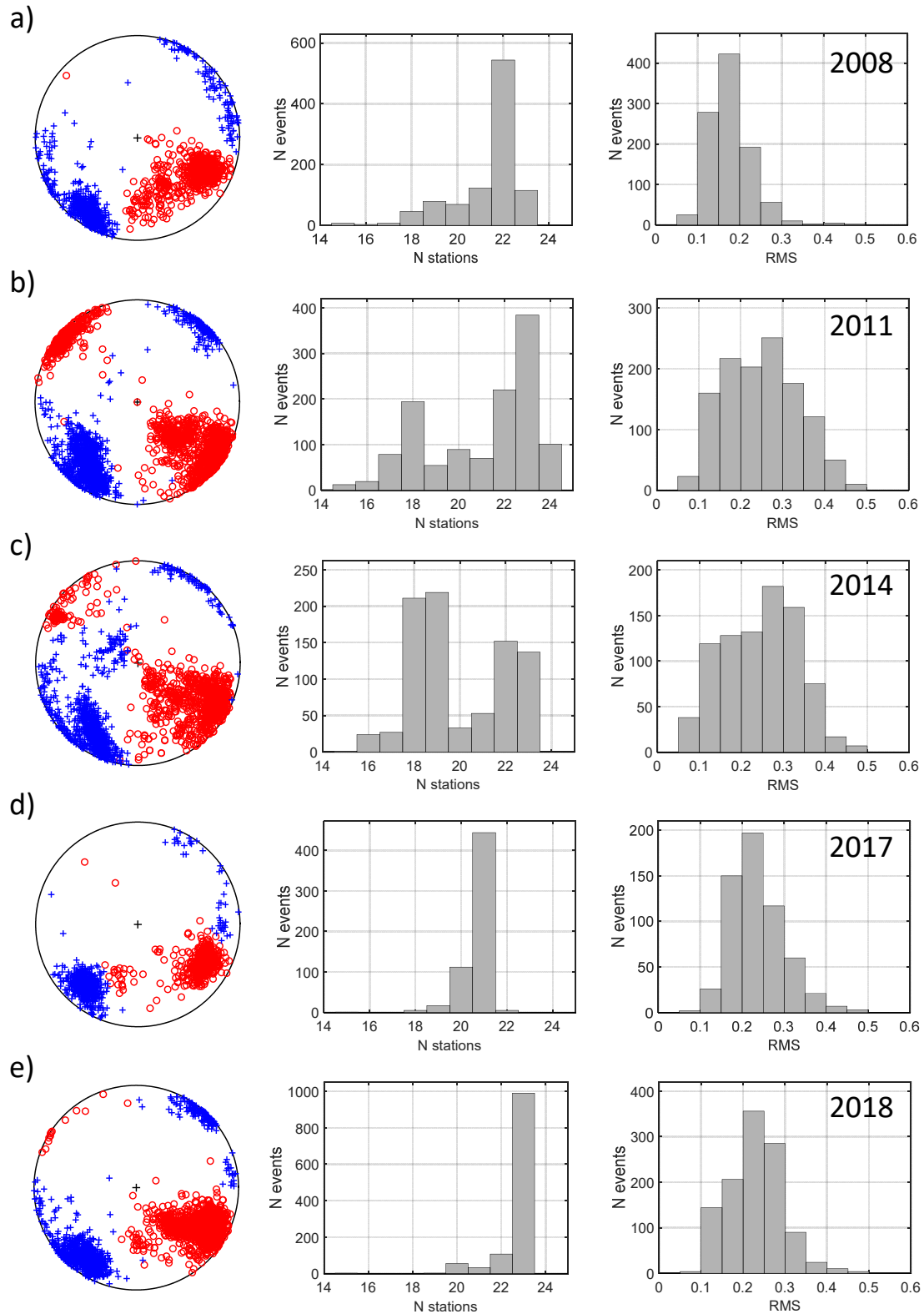


Figure 9. The P/T axes (left-hand plots), histograms of the RMS of the number of stations used in the MT inversion (middle plots), and histograms of the RMS of the retrieved MTs (right-hand plots) for seismic activities in 2008 (a), 2011(b), 2014 (c), 2017 (d) and 2018 (e). N denotes the number of stations, which recorded the individual earthquakes.

601
602
603
604
605
606
607
608
609
610
611
612
613
614
615
616
617
618
619
620
621
622
623
624
625
626
627
628
629
630
631
632
633
634
635
636
637
638
639
640
641
642
643
644
645
646
647
648
649
650
651

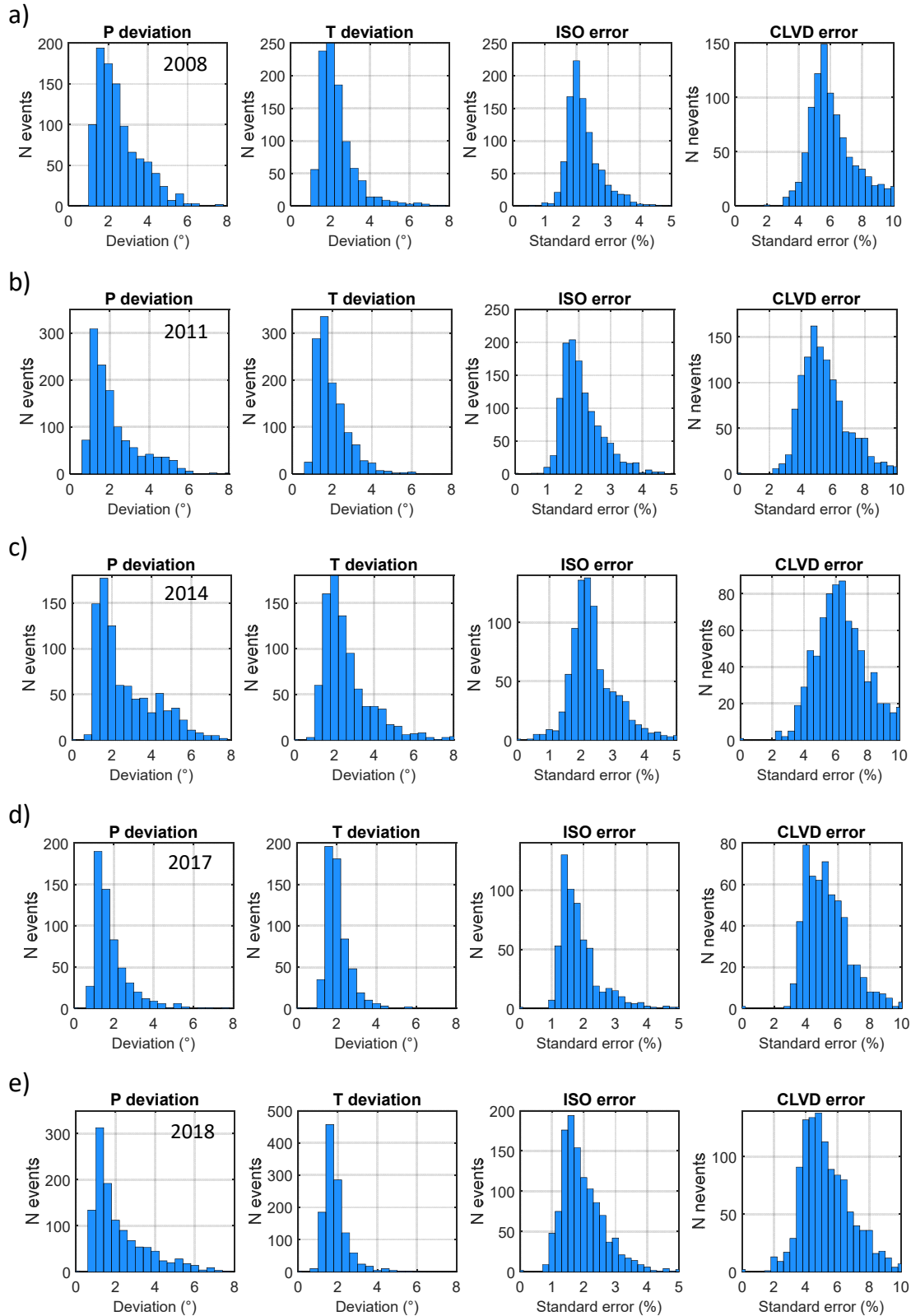


Figure 10. Histograms of mean deviations of the P/T axes and histograms of the ISO and CLVD standard errors for MTs of earthquakes from individual prominent seismic activities: in 2008 (a), 2011(b), 2014 (c), 2017 (d) and 2018 (e). The mean P/T deviations and the ISO and CLVD standard errors were calculated for each event from 100 MTs inverted using randomly generated noisy data.

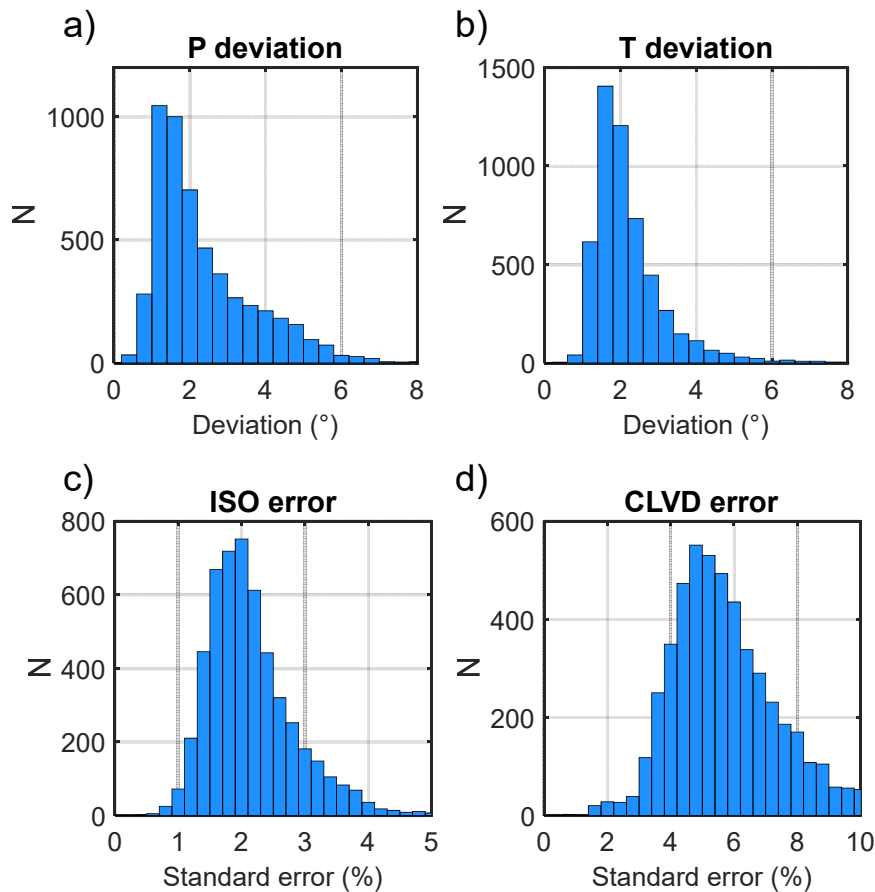


Figure 11. Histograms of mean deviations of the P/T axes (a-b) and histograms of the standard ISO and CLVD errors (c-d) for the 513482 reported MTs. The mean P/T deviations and the ISO and CLVD standard errors were calculated for each event from 100 MTs inverted using randomly generated noisy data.

8 Description of the dataset

The dataset consists of the following directories:

- Waveforms – this directory is further structured into subdirectories according to individual years and earthquakes. Three-component velocity records are stored in ASCII files with four columns (time + 3 components: Z,N,E) individually for each station and each earthquake. The first line of the files contains time of the first sample. The pre-event time before the P-wave arrival is 2s.
- Model – this directory contains the ASCII file ‘model.crust’, which defines the layered velocity model for the West Bohemia region (depth in km, P-wave velocity in km/s, v_P/v_S ratio, P-wave quality factor Q_P and ratio Q_P/Q_S of P-wave and S-wave quality factorsratio).
- Stations – this directory contains the ASCII file ‘stations_Webnet_coordinates.dat’ with coordinates of stations (site, name of the station, latitude, longitude, elevation), file ‘Webnet.xml’ with a full technical specification of stations formatted according to the FDSN StationXML standard (<http://docs.fdsn.org/projects/stationxml/en/latest/>) and file ‘Webnet.dataless’ with a full technical

696 [specification of stations formatted according to the Dataless SEED format](https://ds.iris.edu/ds/nodes/dmc/data/formats/dataless-seed/)
697 [\(https://ds.iris.edu/ds/nodes/dmc/data/formats/dataless-seed/\)](https://ds.iris.edu/ds/nodes/dmc/data/formats/dataless-seed/):-

- 698 • Moments – this directory contains the ASCII file ‘catalogue_2008-2018.dat’ with double difference
699 locations, magnitudes, moment tensors and their errors, RMS and the numbers of inverted stations.
- 700 • Figures – this directory is further structures into subdirectories according to individual years. Four
701 figures are provided for each earthquake [in the .pdf format](#) (see Figure 12): complete waveforms of
702 vertical components, a detail of the P-waveforms, the focal mechanism with positions of stations, and
703 the RMS at individual stations.

704
705 File ‘catalogue_2008-2018.dat’ lists the following quantities for each earthquake:

- 706 • Event identification (composed form year and the sequential number of the event in the year, [e.g.](#)
707 [2008-216](#))
- 708 • Double-difference locations
 - 709 • Origin time (year, day, hour, minute, second)
 - 710 • Latitude (°N)
 - 711 • Longitude (°E)
 - 712 • Depth (km)
- 713 • Local magnitude M_L (calculated according to Horálek et al., 2000)
- 714 • N – number of stations used in the MT inversion
- 715 • Frequencies f_1 a f_2 (in Hz) – ~~optimum-low and high corner frequencies~~parameters of the [optimum](#)
716 Butterworth [4th-order](#) band-pass filter
- 717 • RMS – for its definition, see Equation (1)
- 718 • Moment magnitude M_w
- 719 • Components of the normalized moment tensor: $M_{11}, M_{12}, M_{13}, M_{22}, M_{23}, M_{33}$ (x_1 – North, x_2 – East, x_3
720 – down). The moment tensor is normalized using the Euclidean norm (see Equation 17 of Vavryčuk,
721 2015)
- 722 • Strike1, dip1, rake1, strike2, dip2, rake2 (in °)
- 723 • DC, CLVD, ISO (in %, calculated according to Equations 6-10 of Vavryčuk, 2015)
- 724 • Errors of DC, CLVD, ISO (in %, for the definition of errors, see the text)
- 725 • Deviations of the P/T axes (in °, for the definition of errors, see the text)

726
727

728

729
730
731
732
733
734
735
736
737
738
739
740
741
742
743
744
745
746
747
748
749
750
751
752
753
754
755
756
757
758
759
760
761
762
763
764
765
766
767
768
769
770
771
772
773
774
775

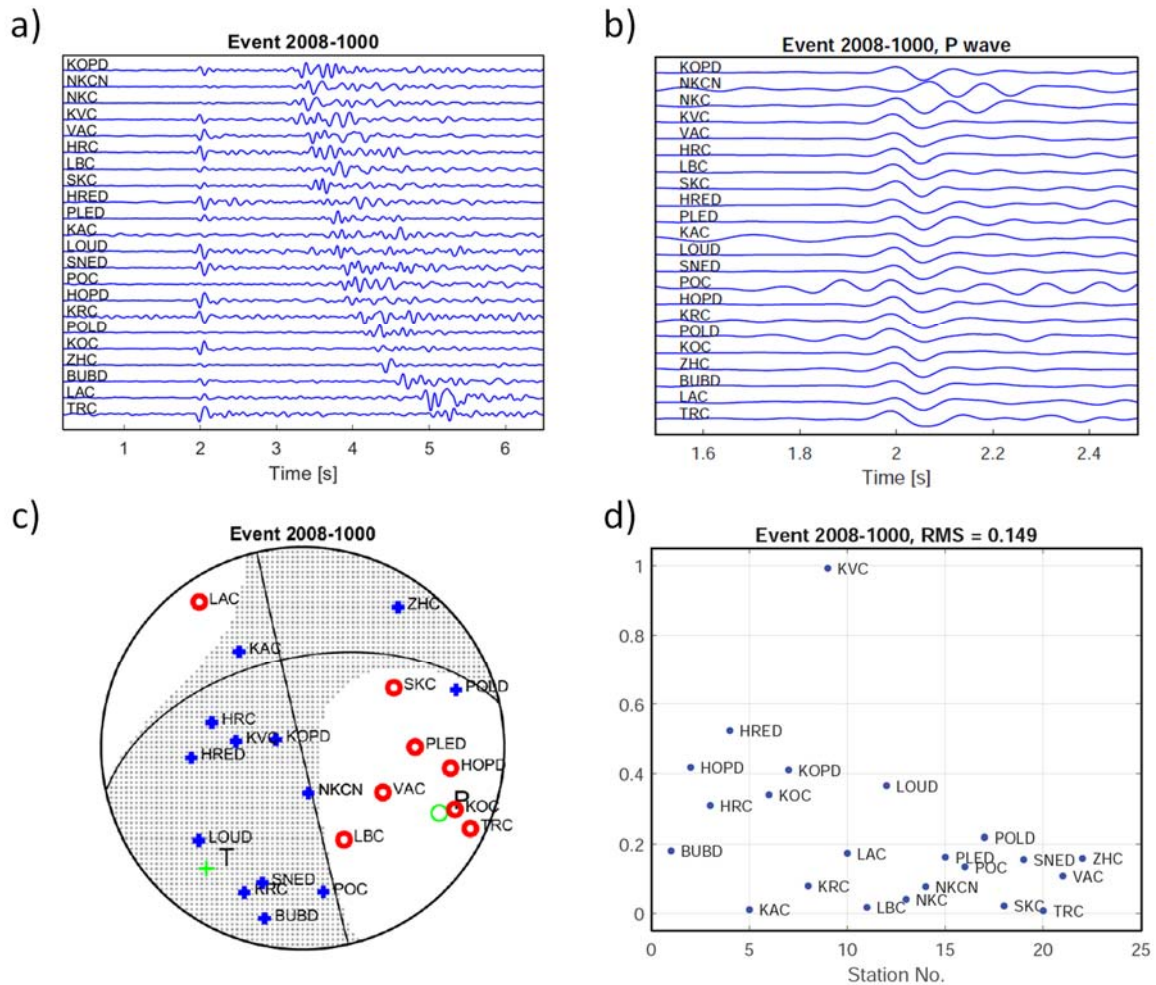


Figure 12. Example of plots provided for each earthquake in the dataset. (a) Vertical components of complete waveforms recorded at the WEBNET stations and aligned according to the arrival time of the P wave. Stations are sorted according to their epicentral distance. (b) Vertical components of the P waves aligned according to their arrival time and with a polarity switched according to the polarity of the common wavelet. (c) The focal mechanism with positions of the stations on the focal sphere (negative polarities – red circles, positive polarities – blue plus signs). (d) Root-mean-squares (RMS) of the differences between the theoretical and observed amplitudes of the P waves.

9 Discussion and conclusions

We publish a unique catalogue of ~~micro~~earthquakes that occurred in the West Bohemia in the period from 2008 to 2018. The catalogue is exceptional in several aspects: (1) it represents an extraordinary extensive dataset of more than 5.000 MTs, (2) it covers a long period of seismicity in the studied area, during which several prominent earthquake swarms took place, (3) the foci locations and retrieved MTs are of a very high accuracy. In addition, the three-component velocigrams recorded at the WEBNET stations together with the velocity model in the region and the technical specification of stations are provided. This predetermines the dataset to be utilized by a large community of researchers for various seismological purposes.

776

777 The great potential of the dataset or its subsets has so far been proved in studies of origins of the swarm activity
778 in this area (Horálek and Fischer, 2008; Fischer et al., 2010; Fischer et al., 2014), migration of seismicity in
779 time due to fluid flow and/or stress redistribution in the focal zone (Hainzl et al, 2012, 2016; Vavryčuk and
780 Hrubcová, 2017), changes of the v_p/v_s ratio in the focal zone (Dahm & Fischer, 2014; Bachura & Fischer,
781 2016), identification of fault segments and their mutual interaction (Vavryčuk and Adamová, 2018; Vavryčuk
782 et al., 2021), the fault instability (Vavryčuk, 2011b, 2014), differences in the seismic energy release in
783 earthquake swarms and mainshock-aftershock sequences (Čermáková and Horálek, 2015; Vavryčuk and
784 Adamová, 2018), the efficiency of new moment tensor inversion algorithms such as the MT inversion based
785 on the PCA (Vavryčuk et al., 2017), the MT inversion using the empirical Green's functions (Vavryčuk and
786 Adamová, 2020). The provided records were also utilized in a study of seismic anisotropy based on the analysis
787 of shear-wave splitting (Vavryčuk and Boušková 2008), identification of shallow discontinuities in the Earth's
788 crust (Hrubcová et al., 2016), lateral variation of depth of the Moho discontinuity (Hrubcová et al., 2013,
789 2017), and for detailed mapping of the non-DC components of MTs and shear-tensile fracturing in the Nový
790 Kostel focal zone (Vavryčuk, 20011a; Vavryčuk et al., 2021).

791

792 The dataset is ideal for being utilized in many other studies in future, e.g., for studies of (1) the interaction
793 between the scattered background regional seismicity and the swarm seismicity focused in the Nový Kostel
794 zone, (2) the Coulomb stress and local stress anomalies connected to fault irregularities, (3) diffusivity of fluids
795 along the activated faults, or (4) time-dependent seismic risk due to the migration of seismicity in the region.
796 In addition, the dataset is optimum for developing and testing new MT inversions (Šílený and Vavryčuk, 2000,
797 2002), stress inversions, and for the spatiotemporal evolution of tectonic stress. Since most of the earthquakes
798 are non-shear, the dataset can contribute to studies of the non-DC components and their relation to shear-tensile
799 fracturing and/or seismic anisotropy in the focal zone (Vavryčuk, 1997; Vavryčuk and Boušková, 2008).

800

801 **Data availability**

802 The MT catalogue and waveforms are available at the Mendeley Dataset Repository
803 <https://doi.org/10.17632/9pwy7rgzkt.1> (Vavryčuk et al., 2022a) and at the International Seismological
804 Centre (ISC) Dataset Repository <https://doi.org/10.31905/H212Z6OX> (Vavryčuk et al., 2022b).

805 ~~The waveforms are available at <https://doi.org/10.17632/4swk36hbvz.1> (Vavryčuk, 2021). For the review~~
806 ~~purpose, the MT catalogue and the other data are available at the following temporary link:~~
807 ~~<https://drive.google.com/drive/folders/1HyFJO6aIwN5SetwsYp-GIhERspeVVz03?usp=sharing>. After the~~
808 ~~acceptance of the paper, the temporary link will be substituted by a permanent doi number accessed under a~~
809 ~~non-restrictive license CC-BY.~~

810

811 **Acknowledgements**

812 The study was supported by the Grant Agency of the Czech Republic, Grant No. 19-06422S. We thank
813 Grzegorz Kwiatek and one anonymous reviewer for their helpful reviews. The moment tensor decomposition

814 [was performed using public open Matlab code MT_DECOMPOSITION \(https://www.ig.cas.cz/en/mt-](https://www.ig.cas.cz/en/mt-decomposition/)
815

816

817

818

819 **References**

- 820 Bachura, M., and Fischer, T.: Detailed velocity ratio mapping during the aftershock sequence as a tool to
821 monitor the fluid activity within the fault plane, *Geophys. J. Int.*, 453, 215-222, 2016.
- 822 Bachura, M., Fischer, T., Doubravová, J., and Horálek, J.: From earthquake swarm to a main shock-
823 aftershocks: the 2018 activity in West Bohemia/Vogtland, *Geophys. J. Int.*, 224(3), 1835-1848, 2021.
- 824 Bankwitz, P., Schneider, G., Kämpf, H., and Bankwitz, E.: Structural characteristics of epicentral areas in
825 Central Europe: study case Cheb Basin (Czech Republic), *J. Geodyn.*, 35, 5-32.
826 [https://doi.org/10.1016/S0264-3707\(02\)00051-0](https://doi.org/10.1016/S0264-3707(02)00051-0), 2003.
- 827 Bath, M.: Lateral inhomogeneities in the upper mantle, *Tectonophysics*, 2, 483–514, 1965.
- 828 Bouchaala, F., Vavryčuk, V., and Fischer, T.: Accuracy of the master-event and double-difference locations:
829 Synthetic tests and application to seismicity in West Bohemia, Czech Republic, *J. Seismol.*, 17(3), 841-
830 859, <https://doi.org/10.1007/s10950-013-9357-4>, 2013.
- 831 Bräuer, K., Kämpf, H., Niedermann, S., and Strauch, G.: Monitoring of helium and carbon isotopes in the
832 western Eger Rift area (Czech Republic): Relationships with the 2014 seismic activity and indications for
833 recent (2000-2016) magmatic unrest, *Chem. Geol.*, 482, 131-145,
834 <https://doi.org/10.1016/j.chemgeo.2018.02.017>, 2018.
- 835 Čermáková, H., and Horálek, J.: The 2011 West Bohemia (Central Europe) earthquake swarm compared with
836 the previous swarms of 2000 and 2008, *J. Seismol.*, 19, 899–913. [https://doi.org/10.1007/s10950-015-](https://doi.org/10.1007/s10950-015-9502-3)
837 [9502-3](https://doi.org/10.1007/s10950-015-9502-3), 2015.
- 838 Červený, V.: *Seismic Ray Theory*. Cambridge University Press, Cambridge, 2001.
- 839 Cesca, S., and Dahm, T.: A frequency domain inversion code to retrieve time-dependent parameters of very
840 long period volcanic sources, *Comput. Geosci.*, 34(3), 235-246, 2008.
- 841 Cesca, S., Buforn, E., and Dahm, T.: Amplitude spectra moment tensor inversion of shallow earthquakes in
842 Spain, *Geophys. J. Int.*, 166, 839-854, 2006.
- 843 Dahm, T., and Fischer, T.: Velocity ratio variations in the source region of earthquake swarms in NW Bohemia
844 obtained from arrival time double- differences, *Geophys. J. Int.*, 196(2), 957-970, 2014.
- 845 Dreger, D., and Woods, B.: Regional distance seismic moment tensors of nuclear explosions, *Tectonophysics*
846 356, 139-156, 2002.
- 847 Fischer, T., Horálek, J., Michálek, J., and Boušková, A.: The 2008 West Bohemia earthquake swarm in the
848 light of the WEBNET network, *J. Seismol.*, 14, 665–682, 2010.
- 849 Fischer, T., Horálek, J., Hrubcová, P., Vavryčuk, V., Bräuer, K., and Kämpf, H.: Intra-continental earthquake
850 swarms in West-Bohemia and Vogtland: a review, *Tectonophysics*, 611, 1-27.
851 <https://doi.org/10.1016/j.tecto.2013.11.001>, 2014.
- 852 Fojtíková, L., Vavryčuk, V., Cipciar, A., and Madarás, J.: Focal mechanisms of micro-earthquakes in the Dobrá
853 Voda seismoactive area in the Malé Karpaty Mts. (Little Carpathians), Slovakia, *Tectonophysics*, 492,
854 213-229, <https://doi.org/10.1016/j.tecto.2010.06.007>, 2010.
- 855 Fojtíková, L., and Zahradník, J.: A new strategy for weak events in sparse networks: The first-motion polarity
856 solutions constrained by single-station waveform inversion, *Seismol. Res. Lett.*, 85(6), 1265-1274,
857 <https://doi.org/10.1785/0220140072>, 2014.
- 858 Ford, S.R., Dreger, D.S., and Walter, W.R.: Network sensitivity solutions for regional moment-tensor
859 inversions, *Bull. Seism. Soc. Am.*, 100(5A), 162-1970, 2010.

860 FeedMeImATroll: Suspension Bridge Picking Algorithm (SBPx)
861 ([https://www.mathworks.com/matlabcentral/fileexchange/51996-suspension-bridge-picking-algorithm-](https://www.mathworks.com/matlabcentral/fileexchange/51996-suspension-bridge-picking-algorithm-sbpx)
862 [sbpx](https://www.mathworks.com/matlabcentral/fileexchange/51996-suspension-bridge-picking-algorithm-sbpx)), MATLAB Central File Exchange, Retrieved September 21, 2021.

863 Frohlich, C.: Earthquakes with non-double-couple mechanisms, *Science*, 264(5160), 804-809, 1994.

864 Hainzl, S., Fischer, T., and Dahm, T.: Seismicity-based estimation of the driving fluid pressure in the case of
865 swarm activity in Western Bohemia, *Geophys. J. Int.*, 191(1), 271-278, 2012.

866 Hainzl, S., Fischer, T., Čermáková, H., Bachura, M., and Vlček, J.: Aftershocks triggered by fluid intrusion:
867 Evidence for the aftershock sequence occurred 2014 in West Bohemia/Vogtland, *J. Geophys. Res.*, 121(4),
868 2575–2590, 2016.

869 Horálek J., Fischer T., Boušková A., and Jedlička P.: The Western Bohemia/Vogtland region in the light of the
870 WEBNET network, *Stud. Geophys. Geod.*, 44(2), 107–125, 2000.

871 Horálek, J., and Fischer, T.: Role of crustal fluids in triggering the West Bohemia/Vogtland earthquake swarms:
872 just what we know (a review), *Stud. Geophys. Geod.*, 52, 455–478, 2008.

873 Hrubcová, P., Vavryčuk, V., Boušková, A., and Horálek, J.: Moho depth determination from waveforms of
874 microearthquakes in the West Bohemia/Vogtland swarm area, *J. Geophys. Res.*, 118, 1–17,
875 <http://dx.doi.org/10.1029/2012JB009360>, 2013.

876 Hrubcová, P., Vavryčuk, V., Boušková, A., and Bohnhoff, M.: Shallow crustal discontinuities inferred from
877 waveforms of microearthquakes: Method and application to KTB drill site and West Bohemia swarm area,
878 *J. Geophys. Res., Solid Earth*, 121, 881-902, <https://doi.org/10.1002/2015JB012548>, 2016.

879 Hrubcová, P., Geissler, W.H., Bräuer, K., Vavryčuk, V., Tomek, Č., and Kämpf, H.: Active magmatic
880 underplating in western Eger Rift, Central Europe, *Tectonics*, 36, <https://doi.org/10.1002/2017TC004710>,
881 2017.

882 Jakoubková, H., Horálek, J., and Fischer, T.: 2014 mainshock-aftershock activity versus earthquake swarms in
883 West Bohemia, Czech Republic, *Pure Appl. Geophys.*, 175(1), 109-131, [https://doi.org/10.1007/s00024-](https://doi.org/10.1007/s00024-017-1679-7)
884 [017-1679-7](https://doi.org/10.1007/s00024-017-1679-7), 2018.

885 Jechumtálová, Z., and Šílený, J.: Amplitude ratios for complete moment tensor retrieval, *Geophys. Res. Lett.*,
886 32, L22303, 2005.

887 Jost, M.L., and Hermann, R.B.: A student's guide to and review of moment tensors, *Seismol. Res. Lett.*, 60,
888 37-57, 1989.

889 Julian, B.R., Miller, A.D., and Foulger, G.R.: Non-double-couple earthquakes 1: Theory, *Rev. Geophys.*, 36,
890 525–549, 1998.

891 Kämpf, H., Bräuer, K., Schumann, J., Hahne, K., and Strauch, G.: CO₂ discharge in an active, non-volcanic
892 continental rift area (Czech Republic): Characterisation (δ C-13, He-3/He-4) and quantification of
893 diffuse and vent CO₂ emissions, *Chem. Geol.*, 339, 71-83,
894 <https://doi.org/10.1016/j.chemgeo.2012.08.005>, 2013.

895 Knopoff, L., and Randall, M.J.: The compensated linear vector dipole: A possible mechanism for deep
896 earthquakes, *J. Geophys. Res.*, 75, 4957-4963, 1970.

897 Kwiątek, G., Martínez-Garzón, P., and Bohnhoff, M.: HybridMT: A MATLAB/Shell environment package for
898 seismic moment tensor inversion and refinement, *Seismol. Res. Lett.*, 87(4), 964-976, 2016.

899 Lay, T., and Wallace, T.C.: *Modern Global Seismology*, Academic Press, New York, 1995.

900 Lomax, A., Michelini, A., and Curtis, A.: Earthquake location, direct, global-search methods, in *Complexity*
901 *In Encyclopedia of Complexity and System Science*, Part 5, Springer, New York, pp. 2449-2473,
902 <https://doi.org/10.1007/978-0-387-30440-3>, 2009.

903 Málek, J., Horálek, J., and Janský, J.: One-dimensional qP-wave velocity model of the upper crust for the West
904 Bohemia/Vogtland earthquake swarm region, *Stud. Geophys. Geod.*, 49, 501-524, 2005.

905 Miller, A.D., Foulger, G.R., and Julian, B.R.: Non-double-couple earthquakes 2: Observations, *Rev. Geophys.*,
906 36, 551-568, 1998.

907 Růžek, B., Vavryčuk, V., Hrubcová, P., Zedník, J. and Celebration Working Group: Crustal anisotropy in the
908 Bohemian Massif, Czech Republic: Observations based on Central European Lithospheric Experiment

909 Based on Refraction (CELEBRATION) 2000, *J. Geophys. Res.*, 108, B8, art. no. 2392, doi:
910 10.1029/2002JB002242, 2003.

911 Šílený, J.: Resolution of non-double-couple mechanisms: Simulation of hypocenter mislocation and velocity
912 structure mismodeling, *Bull. Seism. Soc. Am.*, 99(4), 2265-2272, 2009.

913 Šílený, J., and Milev, A.: Source mechanism of mining induced seismic events - Resolution of double couple
914 and non double couple models, *Tectonophysics*, 456(1-2), 3-15, 2008.

915 Šílený, J., and Vavryčuk, V.: Approximate retrieval of the point source in anisotropic media: numerical
916 modelling by indirect parametrization of the source, *Geophys. J. Int.*, 143, 700-708.
917 <https://doi.org/10.1046/j.1365-246X.2000.00256.x>, 2000.

918 Šílený, J., and Vavryčuk, V.: Can unbiased source be retrieved from anisotropic waveforms by using an
919 isotropic model of the medium? *Tectonophysics*, 356, 125-138, [https://doi.org/10.1016/S0040-1951\(02\)00380-3](https://doi.org/10.1016/S0040-1951(02)00380-3), 2002.

921 Sokos, E., and Zahradník, J.: ISOLA — A Fortran code and Matlab GUI to perform multiple point source
922 inversion of seismic data, *Comput. Geosci.*, 34, 967–977, 2008.

923 Stierle, E., Vavryčuk, V., Šílený, J., and Bohnhoff, M.: Resolution of non-double-couple components in the
924 seismic moment tensor using regional networks: 1. A synthetic case study, *Geophys. J. Int.*, 196(3),
925 1869-1877, <https://doi.org/10.1093/gji/ggt502>, 2014.

926 Stierle, E., Bohnhoff, M., and Vavryčuk, V.: Resolution of non-double-couple components in the seismic
927 moment tensor using regional networks: 2. Application to aftershocks of the 1999 Mw 7.4 Izmit
928 earthquake, *Geophys. J. Int.*, 196(3), 1878-1888, <https://doi.org/10.1093/gji/ggt503>, 2014.

929 Vavryčuk, V.: Elastodynamic and elastostatic Green tensors for homogeneous weak transversely isotropic
930 media, *Geophys. J. Int.*, 130(3), 786-800. <https://doi.org/10.1111/j.1365-246X.1997.tb01873.x>, 1997.

931 Vavryčuk, V.: Weak-contrast R/T coefficients in weakly anisotropic elastic media: *P*-wave incidence, *Geophys.*
932 *J. Int.*, 138, 553-562, doi:10.1046/j.1365-246X.1999.00890.x, 1999. Erratum, *Geophys. J. Int.*, 140
933 (2000), 248, 1999.

934 Vavryčuk, V.: Spatially dependent seismic anisotropy in the Tonga subduction zone: a possible contributor to
935 the complexity of deep earthquakes, *Phys. Earth Planet. Inter.*, 155, 63-72.
936 <https://doi.org/10.1016/j.pepi.2005.10.005>, 2006.

937 Vavryčuk, V.: Real ray tracing in anisotropic viscoelastic media, *Geophys. J. Int.*, 175, 617-626, doi:
938 10.1111/j.1365-246X.2008.03898.x, 2008.

939 Vavryčuk, V.: Tensile earthquakes: Theory, modeling, and inversion, *J. Geophys. Res., Solid Earth*, 116(B12),
940 B12320. <https://doi.org/10.1029/2011JB008770>, 2011a.

941 Vavryčuk, V.: Principal earthquakes: Theory and observations from the 2008 West Bohemia swarm, *Earth*
942 *Planet. Sci. Lett.*, 305, 290-296, <https://doi.org/10.1016/j.epsl.2011.03.002>, 2011b.

943 Vavryčuk, V.: Is the seismic moment tensor ambiguous at a material interface? *Geophys. J. Int.*, 194(1), 395-
944 400, <https://doi.org/10.1093/gji/ggt084>, 2013.

945 Vavryčuk, V.: Iterative joint inversion for stress and fault orientations from focal mechanisms, *Geophys. J. Int.*,
946 199(1), 69-77, <https://doi.org/10.1093/gji/ggu224>, 2014.

947 Vavryčuk, V.: Moment tensor decompositions revisited, *J. Seismol.*, 19(1), 231-252,
948 <https://doi.org/10.1007/s10950-014-9463-y>, 2015.

949 ~~Vavryčuk, V.: WEBNET data 2008-2018, <https://doi.org/10.17632/4swk36hbvz.1>, 2021.~~

950 Vavryčuk, V., and Adamová, P.: Detection of stress anomaly produced by interaction of compressive fault steps
951 in the West Bohemia swarm region, Czech Republic, *Tectonics*, 37, 4212-4225.
952 <https://doi.org/10.1029/2018TC005163>, 2018.

953 Vavryčuk, V., Adamová, P., Doubravová, J., and Jakoubková, H.: Moment tensor inversion based on the
954 principal component analysis of waveforms: Method and application to microearthquakes in West
955 Bohemia, Czech Republic, *Seismol. Res. Lett.*, 88(5), 1303-1315, <https://doi.org/10.1785/0220170027>,
956 2017.

957 Vavryčuk, V., Adamová, P., Doubravová, J., and Ren, Y.: Mapping stress and fluids on faults by nonshear
958 earthquakes, *J. Geophys. Res.: Solid Earth*, 126, e2020JB021287, <https://doi.org/10.1029/2020JB021287>,
959 2021.

960 [Vavryčuk, V., Adamová, P., Doubravová, J., and Horálek, J.: WEBNET moment tensor catalogue 2008-2018,](#)
961 [Mendeley Data, V1, <https://doi.org/10.17632/9pwy7rgzkt.1>, 2022a.](#)

962 [Vavryčuk, V., Adamová, P., Doubravová, J., and Horálek, J.: WEBNET moment tensor catalogue 2008-2018,](#)
963 [ISC Seismological Dataset Repository, <https://doi.org/10.31905/H212Z6OX>, 2022b.](#)

964 Vavryčuk, V., and Boušková, A.: S-wave splitting from records of local micro-earthquakes in West
965 Bohemia/Vogtland: An indicator of complex crustal anisotropy, *Stud. Geophys. Geod.*, 52, 631-650,
966 <https://doi.org/10.1007/s11200-008-0041-z>, 2008.

967 Vavryčuk, V., Bouchaala, F., and Fischer, T.: High-resolution fault image from accurate locations and focal
968 mechanisms of the 2008 swarm earthquakes in West Bohemia, Czech Republic, *Tectonophysics*, 590,
969 189-195, <https://doi.org/10.1016/j.tecto.2013.01.025>, 2013.

970 Vavryčuk, V., and Hrubcová, P.: Seismological evidence of fault weakening due to erosion by fluids from
971 observations of intraplate earthquake swarms, *J. Geophys. Res.*, 122,
972 <https://doi.org/10.1002/2017JB013958>, 2017.

973 Vavryčuk, V., and Kühn, D.: Moment tensor inversion of waveforms: a two-step time-frequency approach,
974 *Geophys. J. Int.*, 190, 1761-1776, <https://doi.org/10.1111/j.1365-246X.2012.05592.x>, 2012.

975 Waldhauser F. and Ellsworth W. L.: A double-difference earthquake location algorithm: Method and
976 application to the northern Hayward fault, California, *Bull. Seismol. Soc. Am.*, 90/6:1353–1368,
977 <https://doi.org/10.1785/0120000006>, 2000.

978 Yu, Ch., Vavryčuk, V., Adamová, P., and Bohnhoff, M.: Moment tensors of induced microearthquakes in The
979 Geysers geothermal reservoir from broadband seismic recordings: Implications for faulting regime, stress
980 tensor and fluid pressure, *J. Geophys. Res., Solid Earth*, 123, 8748-8766,
981 <https://doi.org/10.1029/2018JB016251>, 2018.

982 Yu, Ch., Vavryčuk, V., Adamová, P., and Bohnhoff, M.: Frequency-dependent moment tensors of induced
983 microearthquakes, *Geophys. Res. Lett.*, 46, 6406-6414, <https://doi.org/10.1029/2019GL082634>, 2019.

984 Zahradník, J., Sokos, E., Tselentis, G.-A., and Martakis, N.: Non-double-couple mechanism of moderate
985 earthquakes near Zakynthos, Greece, April 2006; explanation in terms of complexity, *Geophys. Prospect.*,
986 56, 341-356, 2008.

987
988